Electronic Supplementary Materials (ESI)

Cobalt Nanoparticles-embedded Carbon Nanotube/Porous Carbon Hybrid Derived from MOF-encapsulated Co_3O_4 for Oxygen Electrocatalysis

Shuo Dou [a], Xingyue Li [a], Li Tao [a], Jia Huo [a], Shuangyin Wang*, [a], and Liming Dai [b]

Experimental Section

Synthesis of PVP-stabilized Co_3O_4 NPs: The fine-sized Co_3O_4 NPs were synthesized according to the literature described elsewhere.[1] Firstly, 1.6 g cobalt acetate was dissolved in 70 mL benzylamine under stirring for 2 h at room temperature. 70 mL ammonium hydroxide solution was added into the above solution followed by heating in an oil bath at 165 °C for 2 h. Then, diethyl ether was added to precipitate products. The Co_3O_4 NPs were collected by centrifugation and washing with ethanol. The polyvinyl pyrrolidone (PVP) stabilization process was carried out by dispersing Co_3O_4 NPs and PVP (0.6 g Mw=58000) in two beakers with 100 mL chloroform, respectively. Then, two dispersions were mixed under stirring for 24 h. Finally, The PVP-stabilized Co_3O_4 NPs were cleaned with chloroform and hexane to remove the excess PVP and dispersed in methanol and the concentration of PVP-stabilized Co_3O_4 NPs was estimated to be 3 mg mL^{-1}.

Synthesis of Co_3O_4@ZIF-67: 1.642 g 2-methylimidazole (MeIM) was dissolved in 80 mL methanol and 5 mL solution of PVP-stabilized Co_3O_4 NPs was then added under stirring. Another solution with 80 mL methanol and 1.455 g cobalt nitrate hexahydrate was slowly added to the above MeIM solution under stirring for 30 s. The whole mixture was kept at room temperature for 24 h silently. Co_3O_4@ZIF-67 was obtained by centrifugation and washing with ethanol for 5 times and dried at 60 °C in a vacuum oven. Pristine ZIF-67 was also prepared in the absence of Co_3O_4.

Preparation of Co-CNT/PC: Co_3O_4@ZIF-67 was placed in a tube furnace and annealed at 800 °C under N_2 with a heating rate of 5°C min^{-1} for 2 hours. After the tube furnace cooled to room temperature, Co-CNT/PC was obtained. The Co-PC was prepared similar to that of Co-CNT/PC using pristine ZIF-67 as the precursors in the absence of Co_3O_4 nanoparticles.

Synthesis of Co_3O_4@ZIF-8: Co_3O_4@ZIF-8 was synthesized similar to that of Co_3O_4@ZIF-67 except for the use of MeIM (1.3 g) and zinc acetate hexahydrate (0.87 g) as the ligands and metal cores, respectively.

Physical characterizations: Scanning electron microscope (SEM, Hitachi, S-4800) and transmission electron microscope (TEM, FEI, Tecnai G2 F20) were used to observe the morphology of Co-CNT/PC. The X-ray diffraction (XRD) measurements used a Rigaku D/MAX 2500 diffractometer with Cu Kα radiation. X-ray photoelectron spectroscopic (XPS) measurements were carried out with an ESCALAB 250Xi using a monochromic Al X-ray source (200 W, 20 eV). The Brunauer-Emmmett-Teller (BET) specific surface area characterizations of the samples were probed by a nitrogen adsorption−desorption method at 77 K (SSA-4200). Raman spectra were collected on a Raman spectrometer (Labram-010) using 632 nm laser. The thermogravimetric analysis (TGA) was carried out by a STA449C instrument with a heating rate of 5 °C min^{-1} from the 50 to 900 °C in Air.

Electrochemical measurements: To prepare the catalytic ink, 4 mg Co-CNT/PC was dispersed in 2 mL ethanol. After ultrasonication for 30 min, 100 μL 5 % Nafion solution was added to the dispersion followed by ultrasonication for another 30 min. The electrochemical measurements were performed in a three electrodes system using a electrochemical workstation (CHI 760E) and a rotating ring disk electrode apparatus (RRDE-3A, ALS) with Pt mesh as counter electrode and saturated calomel electrode (SCE) as reference electrode. The working electrode for ORR testing was prepared by dripping 10 μL catalytic ink on a glassy carbon (4 mm in diameter) and dried in air. For the OER testing, 500 μL catalytic ink was dripped onto a Ni foam (1×1 cm) to obtain a mass loading of 1 mg cm^{-2}. As the reference, commercial RuO_2 (Aladdin) catalyst was also used to measure the OER performance. All the polarization curves in this study were corrected by *iR*-compensation. Two-electrode rechargeable Zn-air batteries were assembled using Zn plate as anode, Co-CNT/PC supported on carbon paper as cathode, glass fiber filter (Whatman, GF/D) as the separator, and 6 M KOH as the electrolyte, into a mold equipment (MTI, EQ-STC-LI-AIR). To prepare carbon paper supported Co-CNT/PC electrode, 70% electrocatalyst, 20% Super P, and 10% PVDF were dispersed in NMP to get a slurry, coated on a hydrophobic carbon paper (Toray, TGP-H-060) with a catalyst loading ~0.5 mg cm^{-2} and dried at 50 °C for 12 h. We also assembled a reference battery by using a mixture of Pt/C and RuO_2 with an equal loading as electrocatalysts for ORR and OER.

Calculation of transferred electron number (*n*) and H_2O_2 production yield during oxygen reduction reaction

The transferred electron number per oxygen molecule (*n*) involved in ORR was determined by the Koutecky-Levich equation given below:

$$j^{-1} = j_k^{-1} + B^{-1}\omega^{-1/2}$$

Where j_k is the kinetic current and ω is the electrode rotating rate. B could be determined from the slope of the K-L plots in Figure 4c based on the Levich equation as follows:

$$B = 0.2nF(D_{O_2})^{2/3}\nu^{-1/6}C_{O_2}$$

Where n is the number of electrons transferred per oxygen molecule, F is the Faraday constant (F=96485 C mol^{-1}), Do_2 is the diffusion coefficient of O_2 in 0.1 M KOH (1.9×10^{-5} cm^2 s^{-1}), v is the kinetic viscosity (0.01 cm^2 s^{-1}), and Co_2 is the bulk concentration of O_2 (1.2×10^{-6} mol cm^{-3}). The constant 0.2 is adopted when the rotation speed is expressed in rpm.

Rotating ring-disk electrode (RRDE) measurement was also conducted to calculate the transferred electron number (n) as well as the H_2O_2 production yield according to the formulas as follows:

$$n = \frac{4I_D}{I_D + (I_R / \mathrm{N})}$$

$$\mathrm{H_2O_2}\,\% = 100 \times \frac{4-n}{2}$$

where n is the electron transfer number, H_2O_2% is the production yield during the ORR process, I_D is the absolute value of the Faradaic current at the disk, I_R is the absolute value of the ring current, and N is 0.38 in this study.

The RHE calibration was conducted according to the literature. [2] In this study, E (RHE) = E (SCE) + 0.99V.

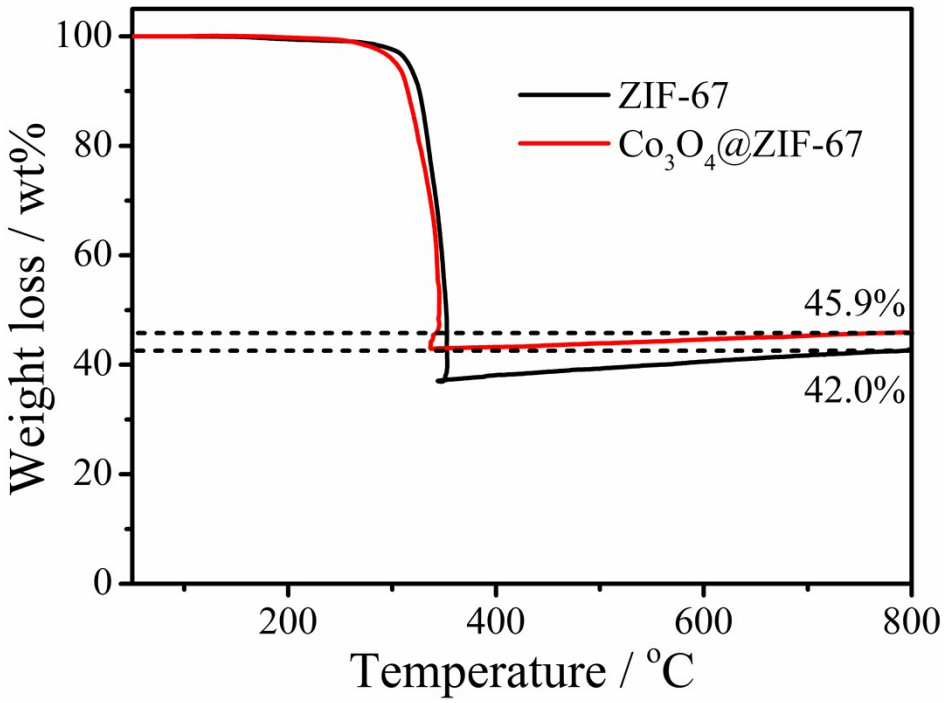

Figure S1. TGA curves of Co_3O_4@ZIF-67 and pure ZIF-67 under Air atmosphere from 50 to 800 °C with a heating rate of 5 °C min^{-1}.

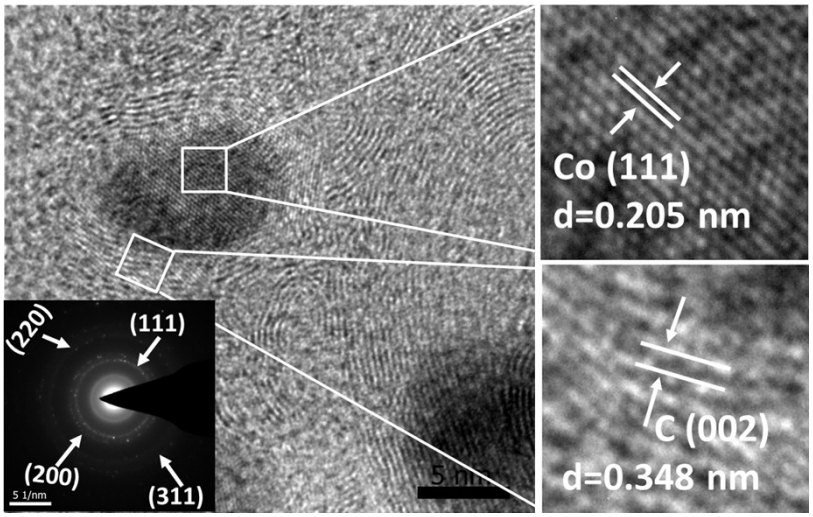

Figure S2. HRTEM image and SAED pattern of Co-CNT/PC with amplified lattice fringes of metallic Co and graphitic carbon.

The high resolution transmission electron microscope (HRTEM) image of Co-CNT/PC in Figure S2 further shows that the lattice fringe spaces of the nanoparticles is 0.205 nm, which is consistent with the (111) plane of metallic Co. The lattice fringes around the Co NPs are measured to be 0.348 nm, and these could be proved to be the (002) plane of carbon, indicating that Co NPs were embedded by graphitic carbon layers instead of being loaded on the surface of carbon layer. The selected area electron diffraction (SAED) patterns in Figure S2 inset also shows several rings which are corresponding to the (111), (200), (220), and (311) diffractions of metallic Co.

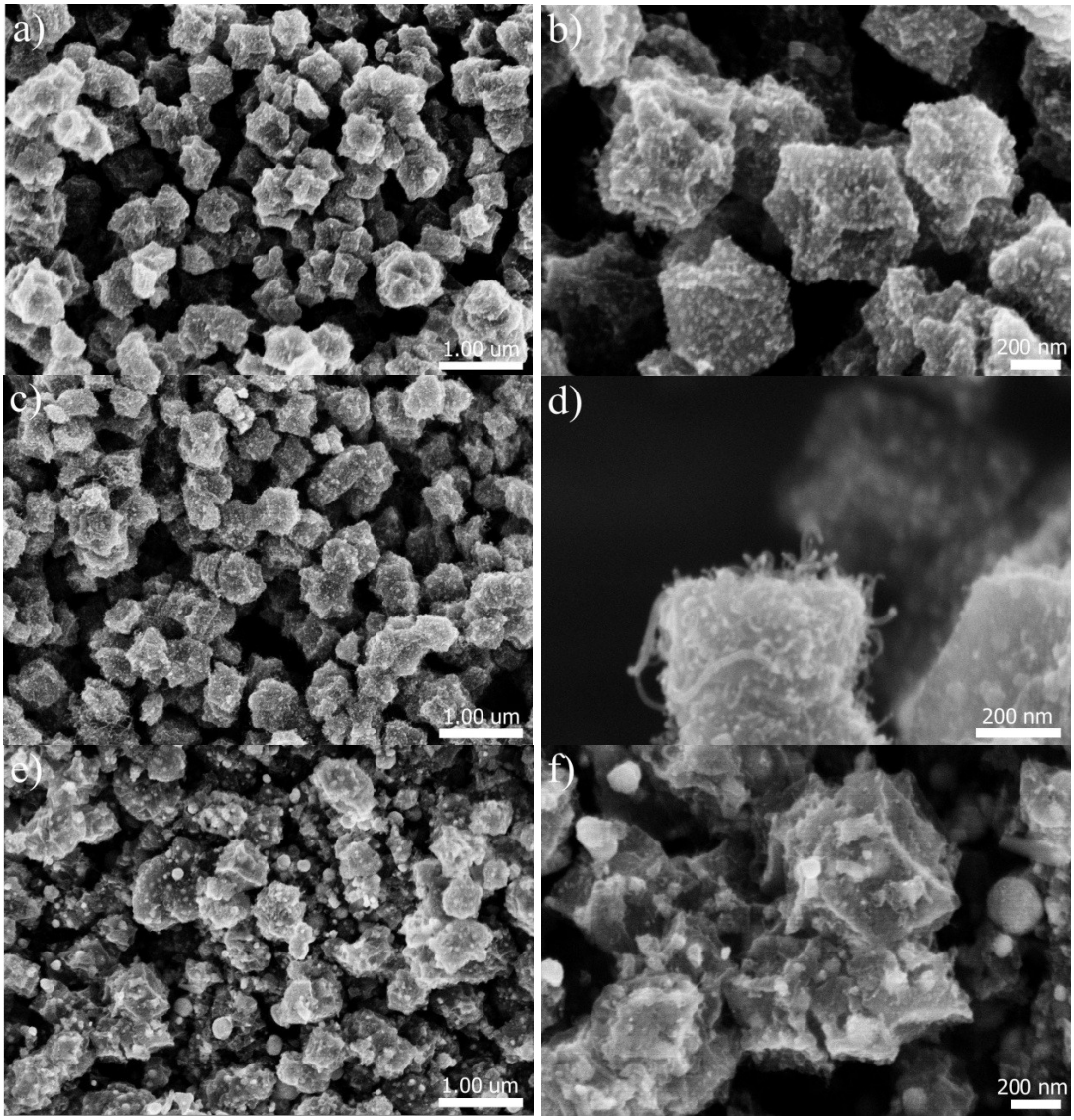

Figure S3. Co_3O_4@ZIF-67 derived Co-CNT/PC at 600 ^oC (a) and (b), there is only a few CNT are obtained; 700 ^oC (a) and (b), more CNT could be obtained at this temperature; 900 ^oC (a) and (b), the whole structure are collapsed at such high temperature.

Temperature is a crucial parameter for the growth of CNTs.[3] Thus, the morphology of pyrolyzed Co_3O_4@ZIF-67 at different temperatures from 600 to 900 °C were examined by SEM in Figure S3. As the temperature increase, more CNTs could be seen, but when the temperature reaches up to 900 °C, the whole MOFs structure collapses and there is scarcely any CNT left, probably due to the fast evaporation of carbon precursor and the weak inter action with catalyst for CNT growth.

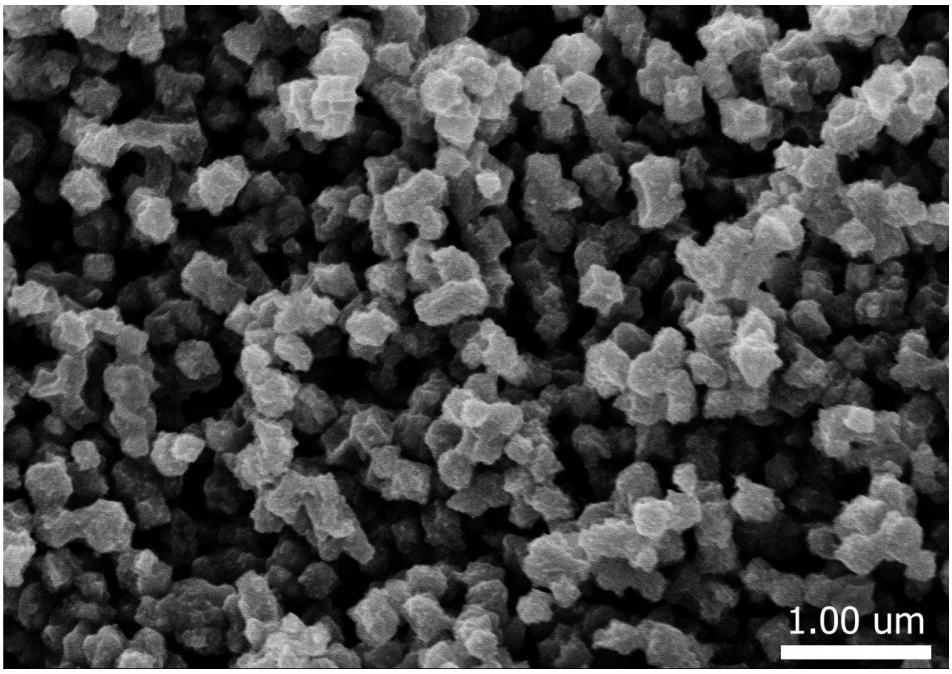

Figure S4. SEM image of pure ZIF-67 derived materials.

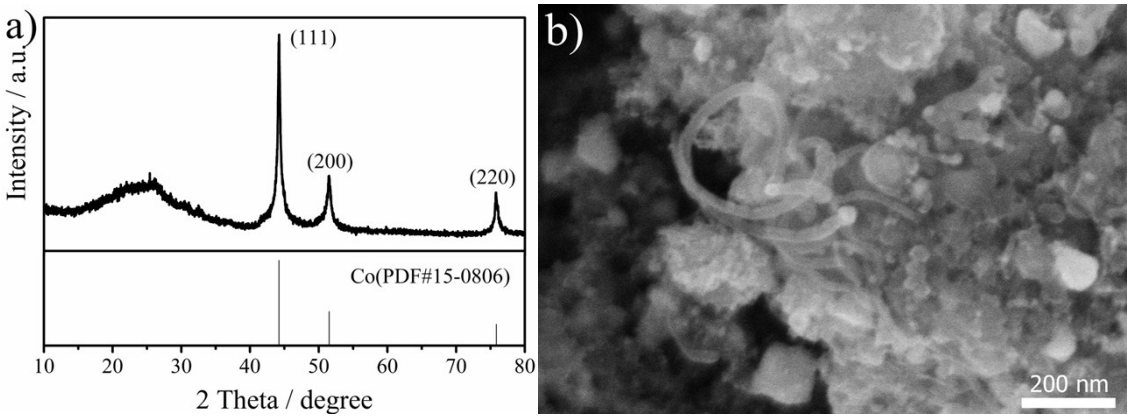

Figure S5. XRD pattern (a) and SEM image (b) of the pyrolyzed mixture of PVP-stablized Co_3O_4 NPs and MeIM.

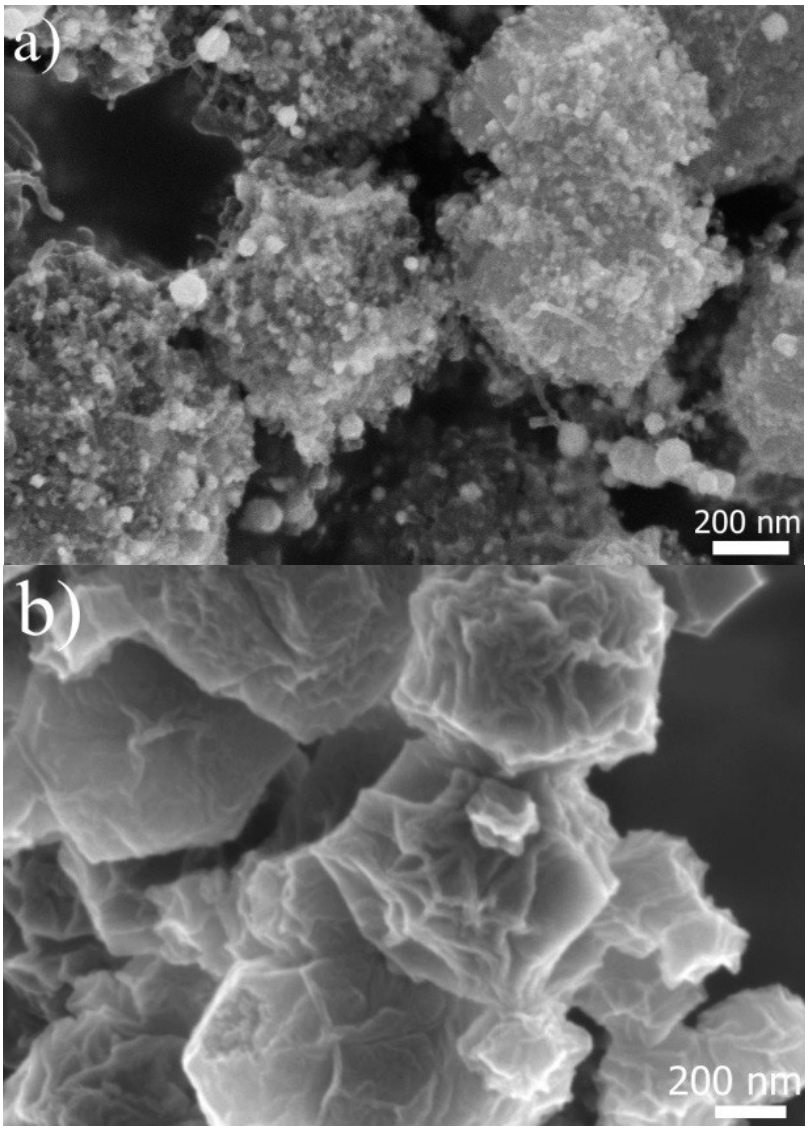

Figure S6. SEM images of Co_3O_4@ZIF-8 (a) and pure ZIF-8 (b) derived materials.

We prepared ZIF-8 (Zn^{2+} as the metal ligand) encapsulated Co_3O_4 NPs followed by pyrolyzing under N_2 at 800 °C. It is found that CNTs do exist in the pyrolyzed Co_3O_4@ZIF-8 (Figure S6a) but not in the pure ZIF-8 (Figure S6b), which indicates that the Co^{2+} in the ZIF-67 is not essential for CNT growth but the pre-loaded Co_3O_4 is.

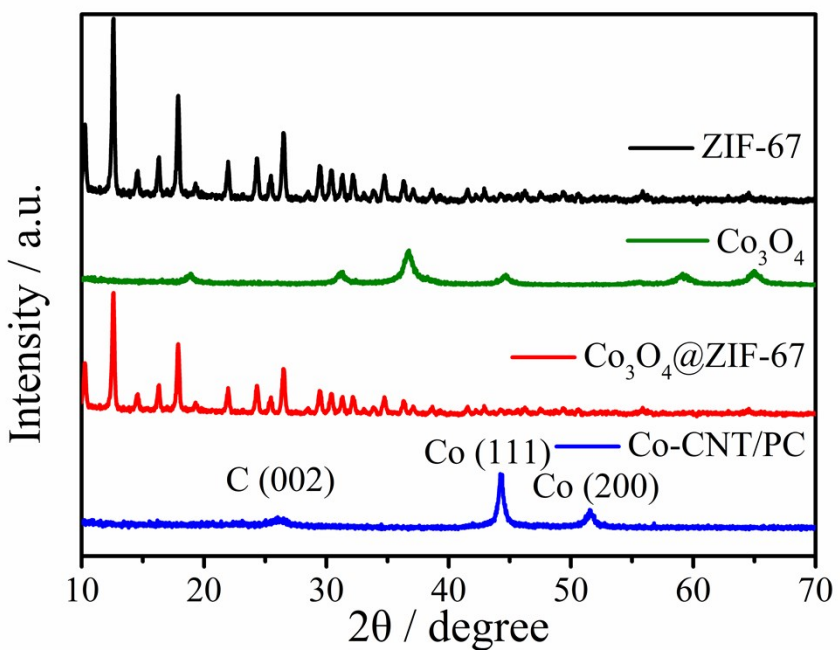

Figure S7. XRD patterns of pure ZIF-67, Co_3O_4, Co_3O_4@ZIF-67, and Co-CNT/PC.

The X-ray diffraction (XRD) measurements were conducted to obtain crystalline structure of pure ZIF-67, Co_3O_4, Co_3O_4@ZIF-67 as well as the as-prepared Co-CNT/PC. As shown in Figure S7, ZIF-67 and Co_3O_4@ZIF-67 patterns agree well with the simulative structure.[4] The pristine Co_3O_4 could also be assigned to the Co_3O_4(PDF#42-1467). In the XRD pattern of Co-CNT/PC, diffraction peaks at 2θ of 44.3° and 51.6° could be assigned to the Co (111) and (200) (PDF#15-0806), which is consistent with the analysis of HRTEM. The characterized signal of carbon could also be seen at 2θ of 26.1° in the Co-CNT/PC and this further confirms the carbonization and formation of carbon matrix.

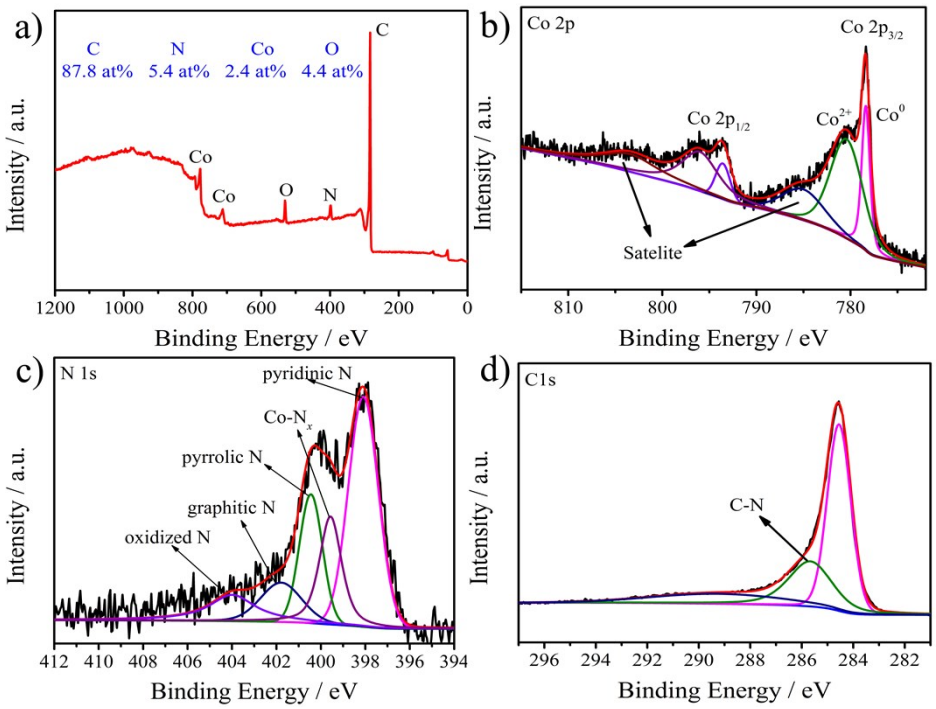

Figure S8. (a) XPS survey spectrum of Co-CNT/PC; (b) the high-resolution Co 2p XPS peak; (c) the high-resolution N 1s XPS peak; and (d) high-resolution C 1s XPS peak.

In order to identify the chemical component of as-prepared Co-CNT/PC, X-ray photoelectron spectroscopic (XPS) measurements were conducted. As shown in Figure S8a, the survey spectrum exhibits that there are four species of C, Co, O, N in the as-prepared Co-CNT/PC at 284.6, 778.4, 532.04, and 399.0 eV, respectively. Figure S8b shows the high-resolution XPS spectrum of Co 2p. Two main peaks at 795.7 and 778.4 eV can be observed which are assigned to Co 2p1/2 and Co 2p3/2. The decovonluted Co 2p3/2 peak suggests that Co-CNT/PC contains metallic Co^0 at 778.4 eV and Co^{2+} at 780.4 eV.[5, 6] Metallic Co comes from the reduction of Co^{2+} and Co_3O_4 NPs during pyrolysis process. The Co^{2+} is attributed to the Co-N_x moieties and the surface oxidation of Co. The Co-N_x moieties were formed by the combination of N atom from decomposed MeIM organic ligand with Co^{2+} during the pyrolysis, and the moieties could provide additional active sites for ORR.[7] The presence of N species is resulted from the decomposed MeIM ligand organic molecule and the N atoms could be doped into the CNT/PC matrix carbon lattice when treated at high temperature which has been confirmed by the high-resolution XPS spectrum of N 1s (Figure S8c) and C 1s (Figure S8d). As identified by high-resolution N 1s XPS peak, four deconvoluted peaks at 398.1, 400.5, 401.8, and 403. 9 eV can be seen which are assigned to pyridinic N, pyrrolic N, graphitic N, and oxidized N, respectively.[8] Previous reports have demonstrated that the presence of pyridinic N could facilitate the ORR performance in carbon materials.[9] It should be noticed that the Co-N_x peak at 399.5 eV could also be found which is consistent with the analysis of Co 2p XPS spectrum. By the way, the presence of O element in the XPS spectrum is probably due to the surface oxidation of metallic Co NPs or the absorbed oxygen species.

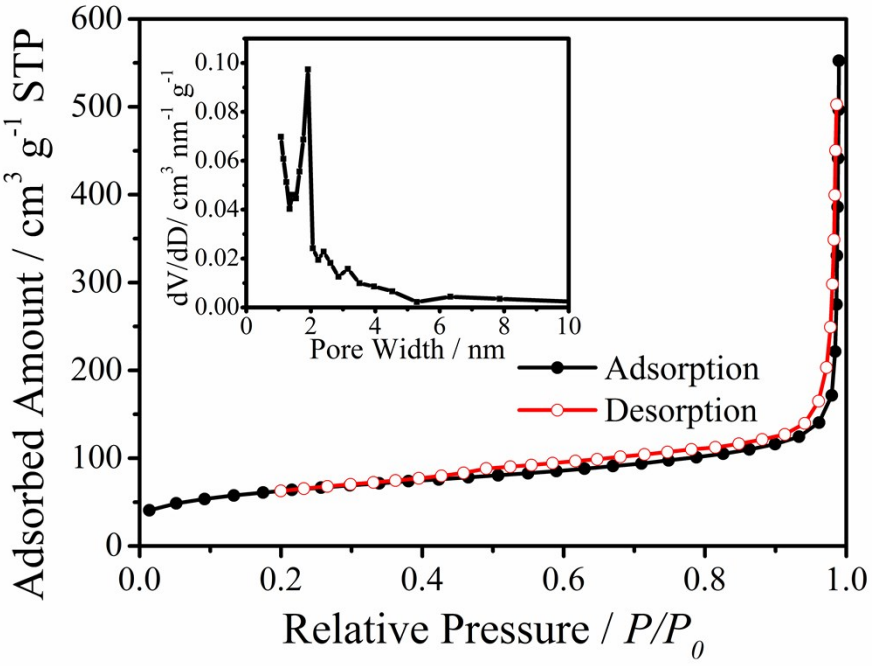

Figure S9. Nitrogen sorption isotherms of Co-CNT/PC (inset: the corresponding pore size distribution)

The N_2 adsorption and desorption isotherm was recorded to analyze the specific surface area and pore size distribution of Co-CNT/PC, as given in Figure S9. A type IV isotherms in Figure 3e suggests that micropore structure exists in the Co-CNT/PC, which is originated from the inheritance of porous ZIF-67.[10] Furthermore, Co-CNT/PC displays a large Brunauer-Emmett-Teller (BET) surface area of 222.9 m^2g^{-1}, which is beneficial for absorbing O_2 and electrolyte ions during electrochemical reactions. The relative Barrett-Joyner-Halenda (BJH) pore size distribution curve in the inset of Figure S9 confirms the microspores centred at ~1.9 nm in Co-CNT/PC. The pores provide excellent O_2 and electrolyte diffusion channel to facilitate the electrocatalytic performance for ORR and OER.

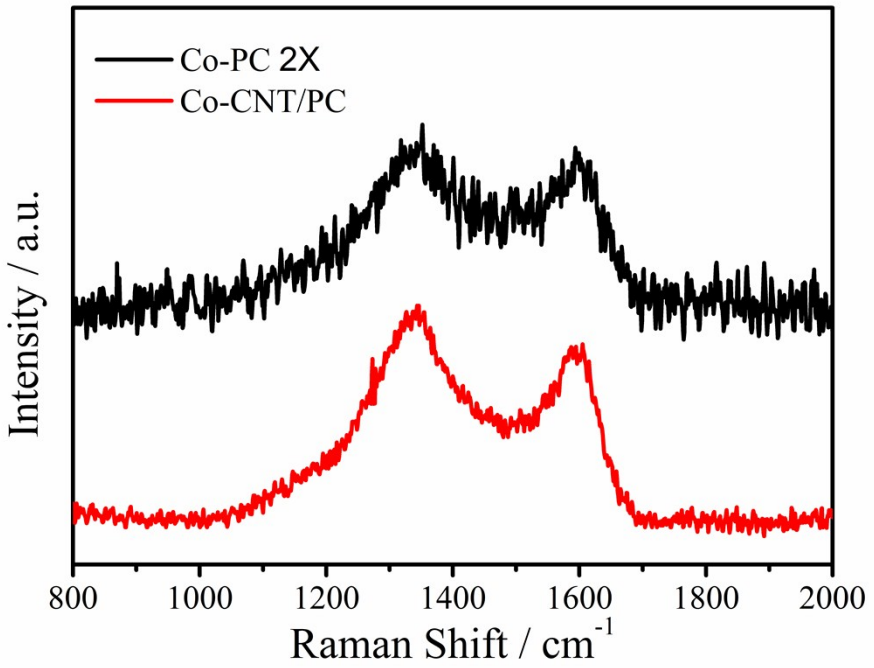

Figure S10. Raman spectra of Co-PC and Co-CNT/PC.

Raman analysis shows that the characteristic peaks of carbon materials, D-bond at 1340 cm^{-1} (corresponding to the disordered or defect carbon) and G-bond at 1590 cm^{-1} (corresponding to the graphitic sp^2-carbon), are present in both Co-PC and Co-CNT/PC. It could be seen that that the Co-PC is more noisy than that of the Co-PC/CNT. This is mainly due to that the pyrolysis method used in this study could result in not well crystalized porous carbon. But in the presence of Co3O4, the crystallinity of obtained PC/CNT became better.

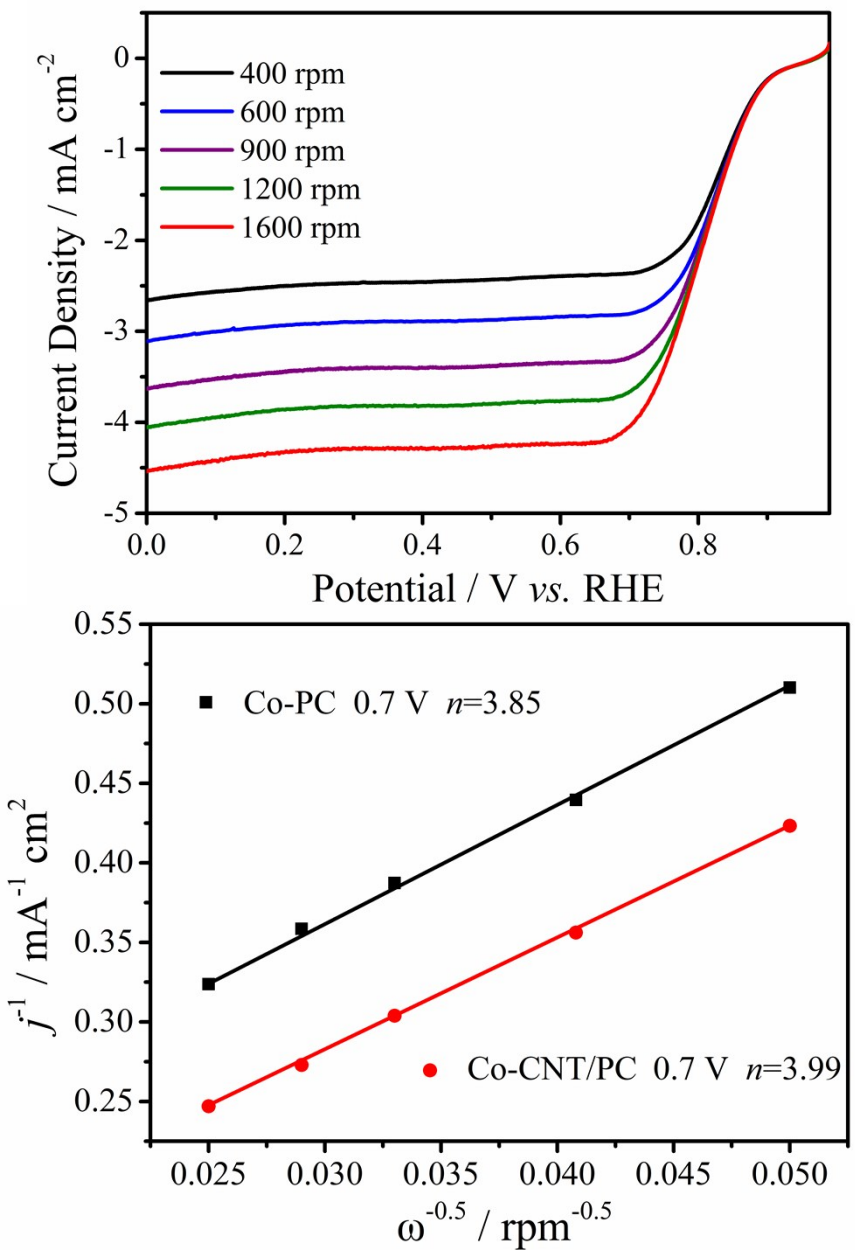

Figure S11.RDE voltammograms of Co-CNT/PC at different rotation rates from 400 to 1600 rpm (a); the Koutecky-Levich plots for the Co-CNT/PC electrocatalysts at 0.7 V vs. RHE (b) .

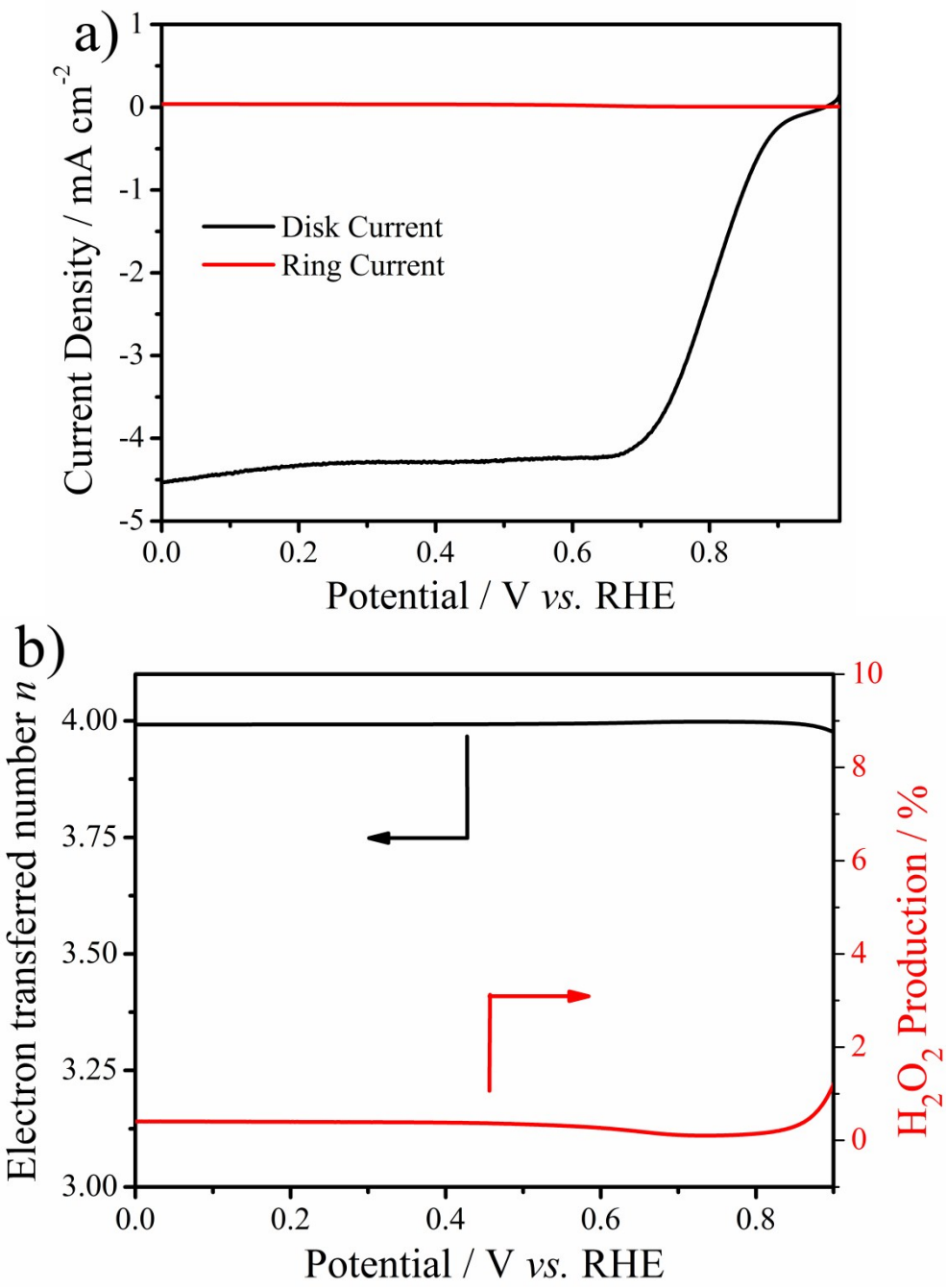

Figure S12. RRDE of Co-CNT/PC in O_2-saturated 0.1 M KOH aqueous solution on the Co-CNT/PC electrode at a rotational speed of 1600 rpm (a); the electron transferred number n and H_2O_2 production yield during oxygen reduction reaction calculated from RRDE (b).

Rotating ring disk electrode (RRDE) test at 1600 rpm was conducted to estimate the ORR performance (Figure S12a). The calculated results in Figure S12b shows that from 0.9 to 1.0 V, the *n* value of Co-CNT/PC remains from 3.97 to 3.99, which is consistent with the result from K-L equation, and the H_2O_2 production yield of Co-CNT/PC electrode is quite low (remains below ~2%).

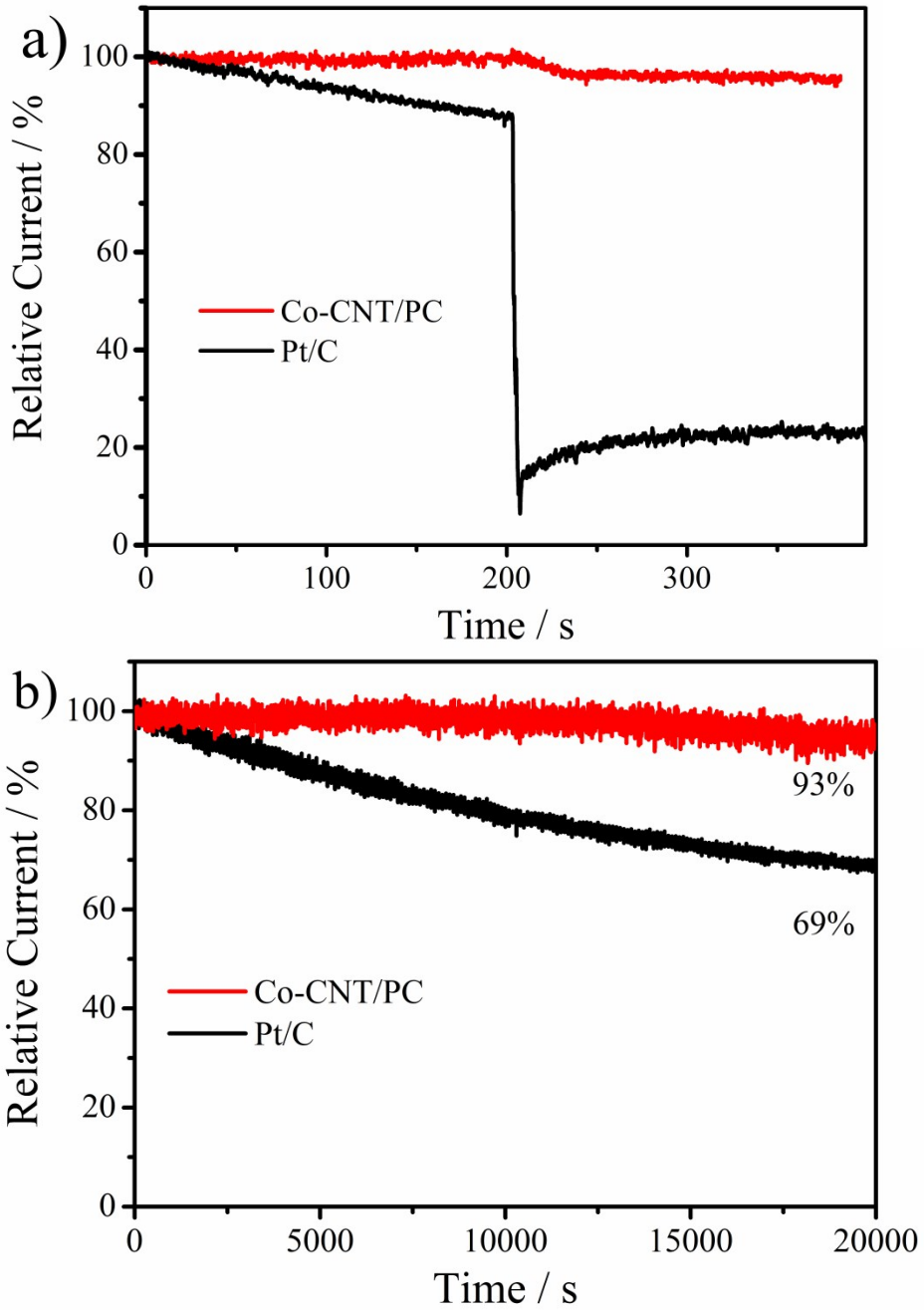

Figure S13. Chronoamperometric responses on Co-CNT/PC and Pt/C electrodes on addition of 1.0 M methanol after about 200s (a); Chronoamperometry test in O_2-saturated 0.1M KOH solution at 0.79 V vs. RHE on Co-CNT/PC and Pt/C for 20000 s.

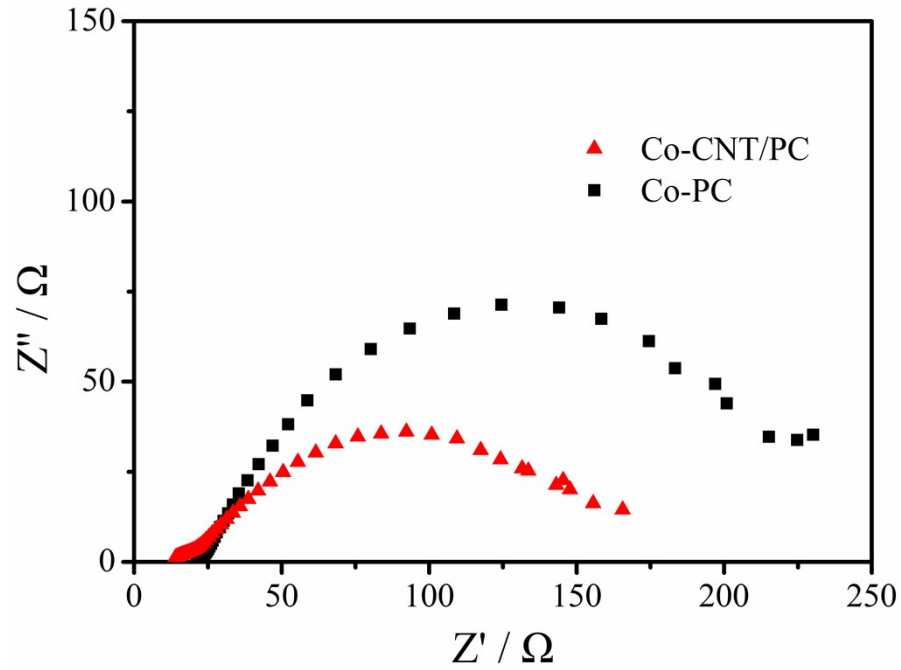

Figure S14. EIS of Co-CNT/PC and Co-PC electrocatalyst at the potential of 1.6 V vs. RHE.

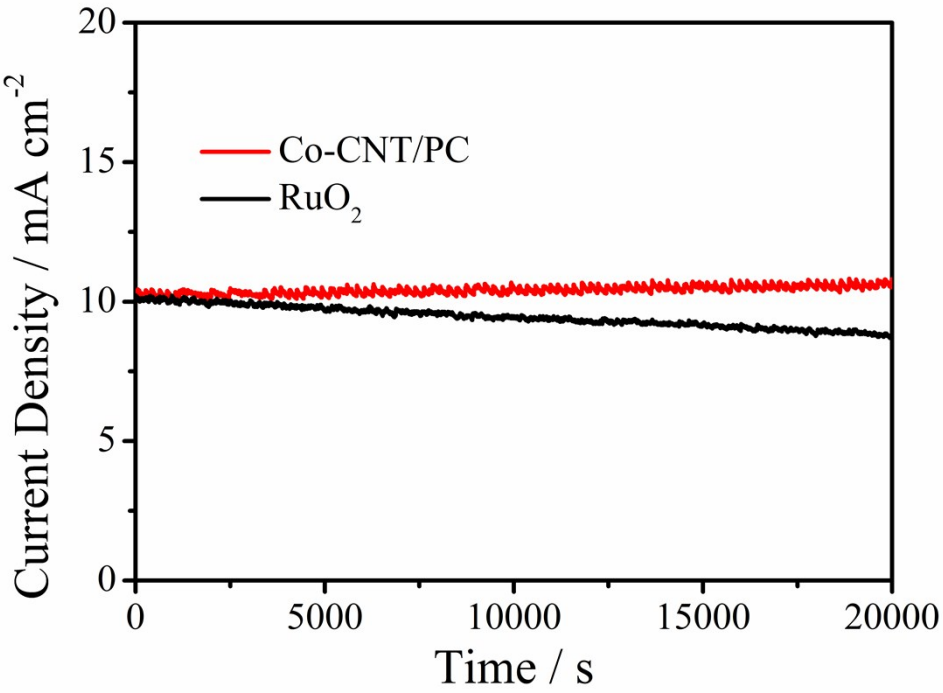

Figure S15. Chronoamperometry test in O_2-saturated 0.1M KOH solution at current density of 10 mA cm^{-2} on Co-CNT/PC and commercial RuO_2 electrodes for 20000 s.

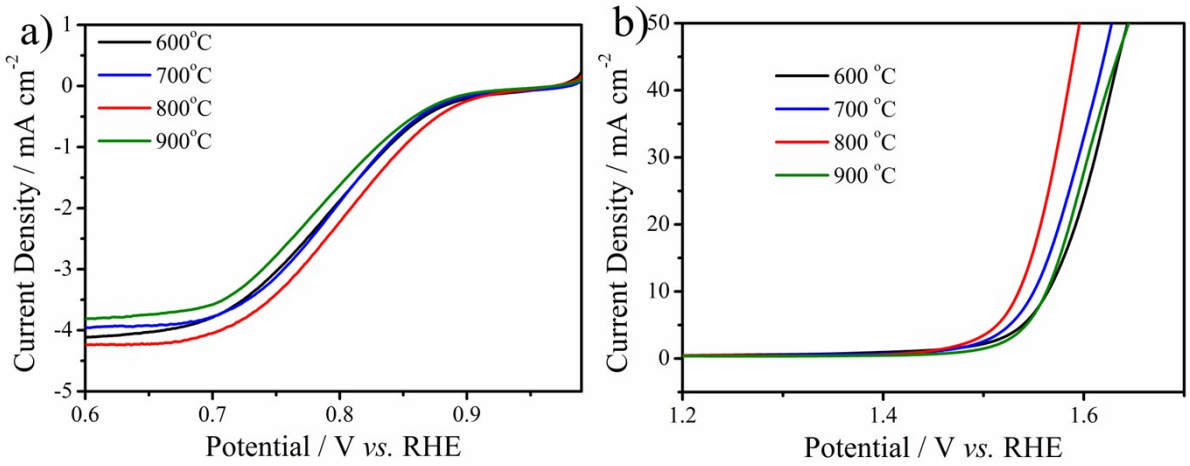

Figure S16. LSV curves of Co-CNT/PC obtained at different in O_2-saturated 0.1M KOH solution for ORR (a) and OER (b).

We investigated the ORR and OER performance of Co_3O_4@ZIF-67 derived-materials obtained at different temperatures from 600 to 900 °C. The results are illustrated in Figure S16. As the temperature increase, improved ORR and OER activity could be observed. While, when the temperature reaches 900 °C, the activities for both ORR and OER are poorer than that of 800 °C. The reason for this is also due to that 800 °C is the optimal temperature to grow CNT, and the more CNT hybridized with ZIF-67-derived porous carbon than 600 and 700 °C could more strongly facilitate the electrical conductivity to improve the electrocatalytic activity. However, 900 °C is too high to obtain an excellent carbonized structure, which would result in the loss of active sites, as evidenced by SEM.

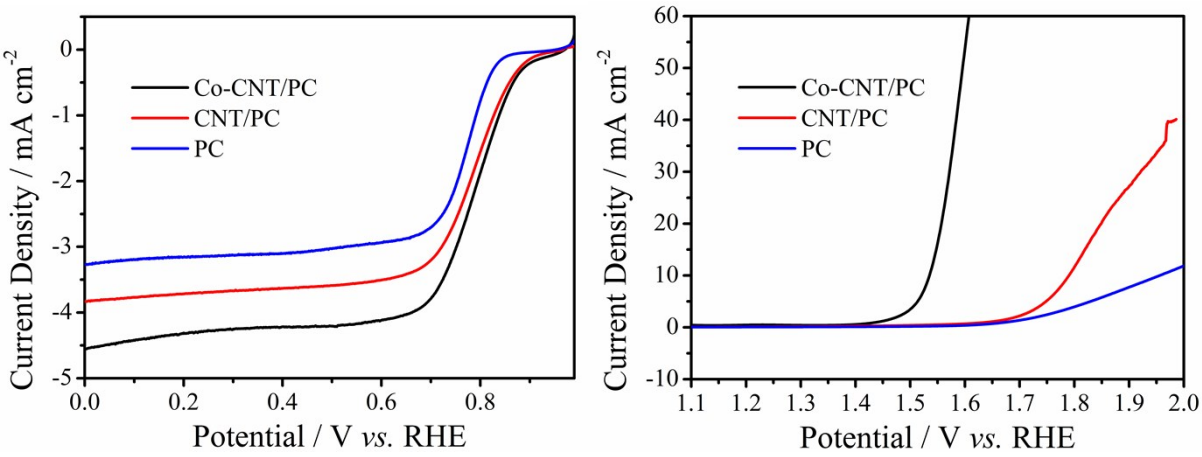

Figure S17. LSV curves of Co-CNT/PC, CNT/PC, and PC in O_2-saturated 0.1M KOH solution for ORR (left) and OER (right). The CNT/PC and PC were obtained by refluxing Co-CNT/PC and Co/PC in 0.5 M H_2SO_4 for 24h at 80 ^oC.

The Co NPs in the Co-CNT/PC and Co-PC could be etched by refluxing the hybrids in 0.5 M H_2SO_4 for 24 h at 80 ^oC, which were denoted as CNT/PC and PC, respectively. It could be seen that after acid leaching, the ORR onset potential of CNT/PC does not show obviously changed compared to the pristine Co-CNT/PC except for the limit current density which is probably due to the lower conductivity after etching Co NPs. Meanwhile, the poorer ORR activity of PC further confirms the important of the existed CNTs. Unlike the ORR performance, CNT/PC electrode shows larger overpotential than that of the Co-CNT/PC and this clearly indicates that the Co NPs in the hybrids play the main role during catalyzing OER.

Figure S18. The optical photograph of rechargeable Zn-air battery with an open circuit potential of 1.37 V using Co-CNT/PC as air electrode.

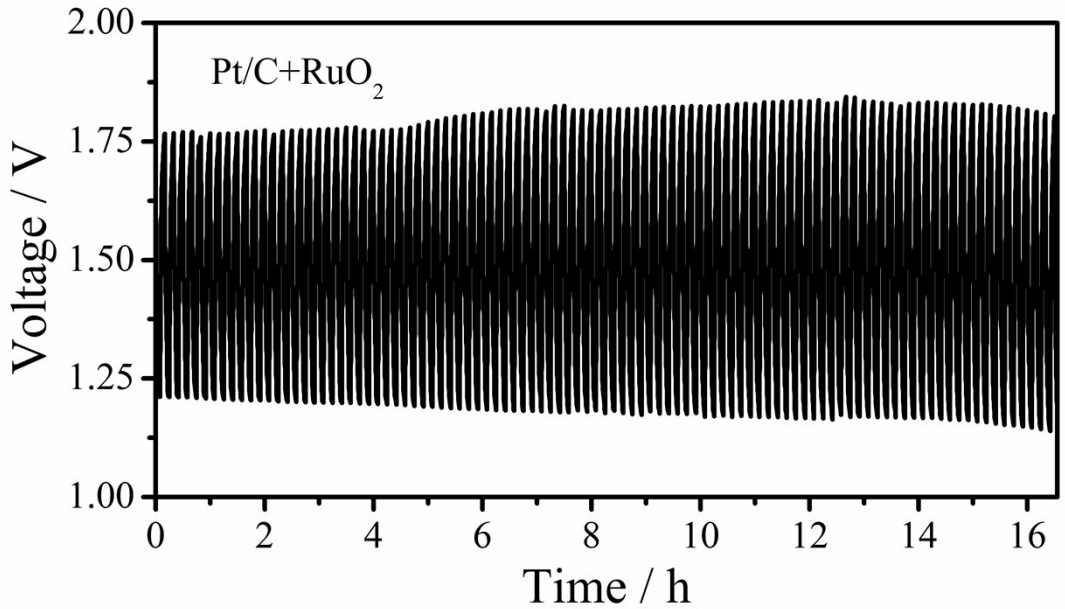

Figure S19. Galvanostatic pulse cycling at 2 mA cm^{-2} for 100 cycles using the mixture of Pt/C and RuO_2 catalyst as the air electrode.

Table S1. Summary of various ZIF-derived carbon-based electrocatalysts for ORR and OER.

Catalysts	Loading for ORR (mg cm^{-2})	Loading for OER (mg cm^{-2})	Onset Potential vs. RHE	*n*	Potential at 10 mA cm^{-2} vs. RHE	Preparation method	Ref.
NCNTFs	0.2	0.2	0.97	3.97	1.60	Pyrolyzing ZIF-67 under Ar/H_2	S11
Carbon-L	0.1	----	0.861	3.68	----	Pyrolyzing ZIF-7 /glucose under Ar	S12
ZIF-67-900	0.36	----	0.91	~3.8	----	Pyrolyzing ZIF-67 under Ar	S13
300nm-MDC	0.4	----	0.86	3.7	----	Pyrolyzing ZIF-67 under Ar	S14
ZIF/rGO-700-AL*	0.4	----	0.93	3.77 ~3.97	----	Pyrolyzing ZIF/GO under Ar and acid leaching	S15
Co-CNT/PC	0.16	1	0.92	3.99	1.54	Pyrolyzing Co3O4@ZIF-67 under N_2	This work

*Footnote: the ORR performance was measured in acid electrolyte.

Comparing the results in the previous studies and this work, we found that the electrocatalytic performance in this work is similar with that in ref. S11. This impresses the important role of CNTs in the hybrid. The ORR onset potential in ref. S11 shows a little positive than that in this work, but the mass loading in this work is less than the work in ref. S11 and the resulted transferred electron number is larger. Thus, we could say that this work represents a significant improvement over the prior work.

References

S1. N. Shi, W. Cheng, H. Zhou, T. Fan and M. Niederberger, *Chem. Commun.*, 2015, **51**, 1338-1340.
S2. Y. Liang, Y. Li, H. Wang, J. Zhou, J. Wang, T. Regier and H. Dai, *Nat. Mater.*, 2011, **10**, 780-786.
S3. Q. Zhang, J. Liu, R. Sager, L. Dai and J. Baur, *Compos. Sci. Technol.*, 2009, **69**, 594-601.
S4. J. Tang, R. R. Salunkhe, J. Liu, N. L. Torad, M. Imura, S. Furukawa and Y. Yamauchi, *J. Am. Chem. Soc.*, 2015, **137**, 1572-1580.
S5. R. Gao, Z. Li, X. Zhang, J. Zhang, Z. Hu and X. Liu, *ACS Cata.*, 2015, **6**, 400-406.
S6. X. Wang, J. Zhou, H. Fu, W. Li, X. Fan, G. Xin, J. Zheng and X. Li, *J. Mater. Chem. A*, 2014, **2**, 14064-14070.
S7. K. Niu, B. Yang, J. Cui, J. Jin, X. Fu, Q. Zhao and J. Zhang, *J. Power Sources*, 2013, **243**, 65-71.
S8. C. Zhang, R. Hao, H. Liao and Y. Hou, *Nano Energy*, 2013, **2**, 88-97.
S9. D. Guo, R. Shibuya, C. Akiba, S. Saji, T. Kondo and J. Nakamura, *Science*, 2016, **351**, 361-365.
S10. H. Zhong, J. Wang, Y. Zhang, W. Xu, W. Xing, D. Xu, Y. Zhang and X. Zhang, *Angew. Chem. Int. Ed.*, 2014, **53**, 14235-14239.
S11. B. Xia, Y. Yan, N. Li, H. Wu, X. Lou and X. Wang, *Nature Energy*, 2016, **1**, 15006.
S12. P. Zhang, F. Sun, Z. Xiang, Z. Shen, J. Yun and D. Cao, *Energy & Environmental Science*, 2014, **7**, 442-450.
S13. X. Wang, J. Zhou, H. Fu, W. Li, X. Fan, G. Xin, J. Zheng and X. Li, *J. Mater. Chem. A*, 2014, **2**, 14064-14070.
S14. W. Xia, J. Zhu, W. Guo, L. An, D. Xia and R. Zou, *J. Mater. Chem. A*, 2014, **2**, 11606-11613.
S15. J. Wei, Y. Hu, Z. Wu, Y. Liang, S. Leong, B. Kong, X. Zhang, D. Zhao, G. P. Simon and H. Wang, *J. Mater. Chem. A*, 2015, **3**, 16867-16873.